Bio-Design and Manufacturing (2026) 9:782–795
https://doi.org/10.1631/bdm.2600114

RESEARCH ARTICLE

Bayesian optimization-enabled efficient embedded ink writing of human tissue analogs

Shanti Quinto[1] · Haoran Cui[1] · Lily Raymond[1] · Eric Shen[2] · Hopson Tan[1] · Liam Bond[1] · Yue Yuan[3] · Bin Duan[4] · Yan Wang[1] · Guangrui Chai[5] · Yifei Jin[1]

Received: 19 February 2026 / Accepted: 29 May 2026 / Published online: 20 July 2026

Abstract

Embedded ink writing has been extensively applied in recent years for various biomedical applications. Despite its outstanding ability to create complex structures, the challenge of optimizing multiple factors has hampered further utilization of this three-dimensional bioprinting strategy. In this work, we experimentally summarized the coupling effects of ink viscosity, support bath rheological properties, and key printing parameters on filament formation. Based on the gathered data, Bayesian optimization is used to establish a filament prediction platform, which can accurately estimate the rheology of support baths for printing alginate-based ink under the given conditions. Additionally, the platform is used to predict the optimal parameters for printing with chitosan ink. Two representative eye-relevant tissues are successfully fabricated using the predictions of the platform. The insights from this study lay the foundation for embedded ink writing strategies that can guide support bath design and identify optimal printing parameters, aiding efficient reconstruction of human tissues and organs in the future.

Graphical abstract

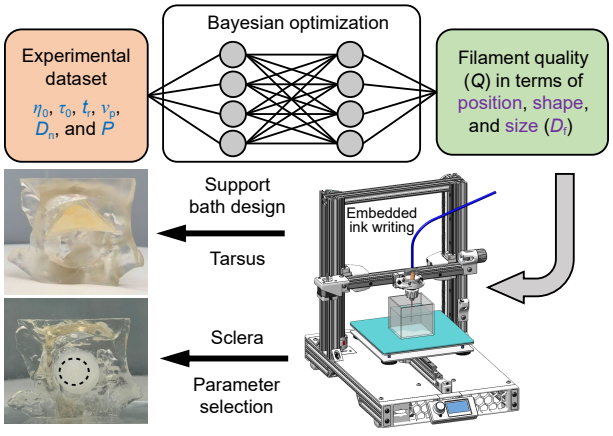

Keywords Bayesian optimization · Embedded ink writing · Support bath design · Three-dimensional (3D) printing parameter prediction · Biomedical applications

Shanti Quinto and Haoran Cui have contributed equally to this work.

✉ Yan Wang
yanwang@unr.edu

✉ Guangrui Chai
chaigr@sj-hospital.org

✉ Yifei Jin
yifeij@unr.edu

[1] Department of Mechanical Engineering, University of Nevada, Reno, Reno, Nevada 89557, USA

[2] Reno High School, Reno, Nevada 89509, USA

[3] Center for Nanophase Materials Sciences, Oak Ridge National Laboratory, Oak Ridge, Tennessee 37830, USA

[4] Mary & Dick Holland Regenerative Medicine Program, Division of Cardiovascular Medicine, Department of Internal Medicine, University of Nebraska Medical Center, Omaha, Nebraska 68198, USA

[5] Department of Ophthalmology, Shengjing Hospital of China Medical University, Shenyang 110004, China

1 Introduction

Embedded ink writing (EIW), a material extrusion three-dimensional (3D) printing strategy, has been rapidly developed and extensively utilized in the past few years [1–3]. In EIW, ink material is printed into 3D structures within a liquid support bath, where the surrounding medium provides both omnidirectional mechanical support and a biologically relevant environment. This unique configuration makes EIW particularly well-suited for printing cellular constructs and other complex architectures for biomedical applications [4, 5].

During EIW, the coupling effects of three main factors—ink viscosity, support bath rheology (such as yield stress and thixotropic response time), and key printing parameters—lead to the formation of various filament types [4, 6, 7]. Specifically, ink viscosity governs the flow behavior of the material during extrusion and its structural stability after deposition, which affects the selection of printing parameters and the design of the support bath. During extrusion, high-viscosity inks typically require a higher dispensing pressure, a larger nozzle diameter (particularly for cell printing applications), and a relatively lower path speed in order to prevent filament breakup and flow instability. After extrusion, the filaments formed from high-viscosity inks are better able to retain their geometry, reducing susceptibility to undesired upward flow along the crevasse generated by nozzle movement. As a result, support baths with relatively long thixotropic response times can still maintain printing fidelity under such conditions.

The rheological properties of the support bath also affect the printing parameters, and are influenced by ink viscosity. Notably, yield stress serves two critical functions in EIW. (1) During printing, sufficient yield stress is required to stabilize deposited filaments and resist drag forces induced by nozzle motion; this enables the formation of well-defined filaments with diameters comparable to or smaller than the nozzle's inner diameter. After printing, an adequate yield stress helps preserve filament position and shape, eliminating unwanted filament shrinking within the support bath. Thus, a high yield stress is expected for high-speed EIW [1]. (2) Thixotropic response time primarily influences the support bath behavior during printing by governing the timescale over which the bath material transitions from a fluid-like state to a solid-like state following shear. Importantly, a longer thixotropic response time may be advantageous for low-viscosity inks printed at high speeds because extended fluidization facilitates the closure of the nozzle-induced crevasse, thereby minimizing unwanted upward flow and improving filament stability.

In EIW, only a few types of filaments have well-defined morphologies and controllable geometries that can be used to print 3D structures [8, 9]. Identifying the optimal conditions to form these filaments is labor-intensive and typically relies on trial and error. In particular, rapid screening for optimal factor combinations is extremely challenging when printing new inks and/or operating under specific printing constraints [10–12]. Therefore, it is vital to develop predictive platforms that can efficiently guide the design of support baths and the selection of printing parameters, enabling the generation of well-defined filaments.

Recently, machine learning techniques have been integrated with diverse 3D printing strategies for real-time assessment of printed products [13], modulation of printing processes [14], structural design assistance [15], planning of printing trajectories [16], and other related applications. However, utilizing machine learning for filament prediction in EIW remains largely unexplored, mainly because of the complicated coupling effects among ink, the support bath, and printing parameters, which lead to less accurate results. In this work, we selected yield stress (τ_0) and thixotropic response time (t_r) as two classic support bath rheological properties, and controlled three key printing parameters—path speed (v_p), nozzle diameter (D_n), and dispensing pressure (P)—in order to print diverse filaments from inks with different viscosities (η_0). Based on the position-shape-size (PSS) evaluation system published in a previous study [4], these filaments were assessed and categorized, as shown in Fig. 1a. This collection of data was further leveraged in the Bayesian optimization to establish a filament prediction platform (Fig. 1b). To validate the efficiency of the platform, we used it to design a support bath for printing tarsus structures from alginate-based ink, as well as to select optimal printing parameters for producing sclera structures from chitosan ink, as illustrated in Fig. 1c. The goal of the proposed platform is to replace current trial-and-error approaches, providing an efficient method to optimize the key factors of EIW for future biomedical applications.

2 Results and discussion

2.1 Filament printing and evaluation via the PSS system

By utilizing varying combinations of ink, support baths, and printing parameters, over one thousand filaments were printed for this study, demonstrating diverse morphologies and geometries. A well-established PSS system [4] was utilized to assess and categorize these filaments. Specifically, the filament position was first qualitatively evaluated by comparing the equilibrium position of a deposited filament with its initial placement, as depicted in Fig. 2a. A suitable support bath must exhibit sufficient τ_0 to maintain the filament in situ after deposition, enabling stable layer-by-layer stacking along predefined trajectories, and thus the fabrication of

well-organized 3D structures. If the support bath cannot fully counteract the downward extrusion force, the deposited filament gradually moves to the bottom and stops below the initial placement, resulting in the formation of sinking filament (encoded as 1.0 in this work).

Following assessment of the position, we focused on evaluating the filament morphology from two aspects. One was the filament's overall shape, as illustrated in Fig. 2b1. Mismatches between ink and bath materials [17–20], unsuitable printing parameters [21–23], and undesired ink–bath interactions [18, 19, 24] typically lead to the formation of filaments with irregular shapes, such as twisted, broken, and discontinuous filaments (encoded as 2.1, 2.3, and 2.4 in this work, respectively). These filaments are unsuitable for reliable printing applications. The other aspect was the cross-sectional shape, which was assessed by measuring key geometric dimensions. The aspect ratio (ranging from 0.5 to 0.7 [4]) can be calculated as a quantitative metric for

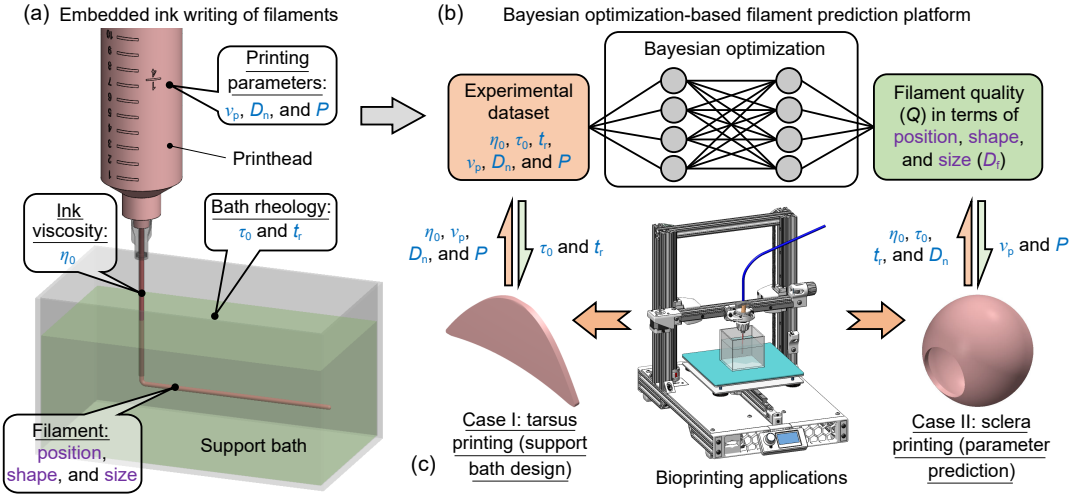

Fig. 1 Research outline. (a) Embedded ink writing and the three key factors which collectively affect filament morphology and geometry—ink viscosity, support bath rheological properties, and printing parameters. (b) Establishment of a Bayesian optimization-based filament prediction platform. (c) Efficient design of a support bath (Case I) and rapid prediction of printing parameters (Case II) using the platform

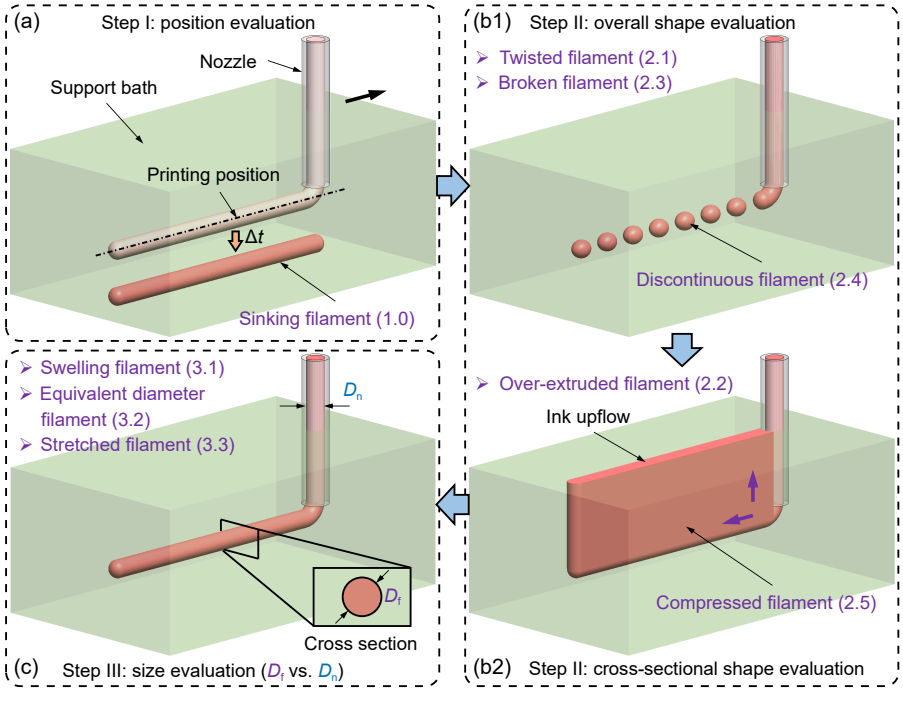

Fig. 2 Assessment of printed filaments via the established position-shape-size (PSS) system. (a) Evaluation of filament position compared to the initial printing position. Evaluation of overall shape (b1) and cross-sectional shape (b2) of printed filaments. (c) Quantification of filament diameter in comparison to nozzle inner diameter

filament cross-sectional fidelity. Two representative filaments include over-extruded filament (encoded as 2.2) and compressed filament (encoded as 2.5), as illustrated in Fig. 2b2. Both of these filaments possess relatively well-defined overall shapes, but their uncontrollable cross-sectional geometries make them inappropriate for construction of high-resolution 3D structures.

Finally, quantitative evaluation using D_n as a reference metric was performed on filaments that satisfied both the position and shape criteria. Filament size, as quantified by the filament diameter (D_f) in Fig. 2c, is of great significance since it directly affects other key parameters in EIW (such as inter-filament distance and layer height). Generally, D_f is determined by the counterbalance between v_p and the ink extrusion speed (v_{ink}) [25–27]. When $v_p<v_{ink}$, more ink material is accumulated during printing, resulting in the formation of a swelling filament (encoded as 3.1) with D_f exceeding D_n. When v_p is approximated as v_{ink}, the dragging effect causes a reduction in D_f, making it equivalent to D_n. Thus, the resultant filament is termed the "equivalent diameter" filament and was encoded as 3.2 in this work. When $v_p>v_{ink}$, the dragging effect becomes pronounced, causing D_f to be less than D_n. This type of filament is therefore termed the "stretched" filament and was encoded as 3.3. Using this PSS system, the collected filaments were systematically analyzed and categorized into different codes.

2.2 Establishing a Bayesian optimization-based filament prediction platform

Using the filament datasets, we established a Bayesian optimization-based filament prediction platform (hereafter referred to as the BO platform). BO was selected as the machine learning approach for the following reasons. First, EIW involves a high-dimensional, nonlinear, and experimentally expensive design space. Generating each new data point requires material preparation, rheological characterization, and embedded printing tests. BO, on the other hand, is particularly well suited for this scenario because it enables sample-efficient optimization of expensive black-box functions. Unlike traditional trial-and-error approaches, BO combines a surrogate model with an acquisition function to balance the exploration of uncertain regions and the exploitation of promising conditions, thereby minimizing the number of experiments needed to identify optimal parameters. This capability is especially valuable for our work, which aims not only to model existing data but also to efficiently guide the selection of support bath formulations and printing parameters. Second, BO offers several practical advantages over other machine learning approaches, such as random forests, support vector machines, and artificial neural networks [28–30]. For example, BO naturally incorporates predictive uncertainty, which is critical when data are limited relative to the dimensionality of the parameter space. Additionally, BO is inherently aligned with process optimization rather than prediction or classification individually. In this context, BO is not merely a regression tool, but a decision-making framework that can help recommend promising experimental conditions for accelerated optimization.

In the BO platform, the optimization objective is to maximize the filament quality, as quantified by a scalar metric $Q\in[0, 3.3]$, where $Q=0$ represents severe filament defects (i.e., failures of position, shape, and size) while $Q>3.0$ represents an ideal filament with excellent structural fidelity. The BO platform enables efficient navigation of the high-dimensional parameter space associated with the ink viscosity, support bath rheological properties, and various printing parameters. These parameters and their role in filament formation during EIW are summarized in Table 1.

BO is implemented using a Gaussian process surrogate model to approximate the nonlinear relationships between the hyperparameters and the filament quality. Each filament printing experiment provides a data pair (X_i, Q), where X_i denotes a specific combination of the six parameters above. The Gaussian process surrogate formulates a predictive distribution of filament quality, providing both a mean estimate $\mu(X_i)$ and an associated uncertainty $\sigma(X_i)$, and thereby enabling informed decision-making in underexplored regions of the design space. The expected improvement (EI) acquisition function is applied to identify the next experimental condition, thus simultaneously balancing exploration (i.e., sampling uncertain regions with high $\sigma(X_i)$) and

Table 1 A list of parameters in embedded ink writing (EIW) used in the Bayesian optimization

Hyperparameter	Physical parameter	Significance
Y	Filament quality (Q)	Position, shape, and size of the printed filament
X_1	Yield stress (τ_0)	The support bath's ability to mechanically stabilize the extruded filament and maintain its geometry
X_2	Thixotropic response time (t_r)	The support bath's ability to recover its status and fill the air gap behind the nozzle translation
X_3	Path speed (v_p)	Nozzle movement speed to affect filament quality
X_4	Nozzle diameter (D_n)	Nozzle inner diameter to directly determine ink extrusion speed and affect filament quality
X_5	Pressure (P)	Dispensing pressure to directly determine ink extrusion speed and affect filament quality
X_6	Ink viscosity (η_0)	Zero-shear-rate viscosity of the ink material to quantify extrudability

exploitation (i.e., sampling near combinations already known to produce high Q values). For example, at iteration k, the next input $X_i(k+1)$ is selected by maximizing the EI function: $\alpha_{\mathrm{EI}}(X_i)=E[\max(0, Q^*-Q)]$, where Q^* is the best filament quality observed so far. The acquisition function is optimized with a multi-start gradient-based approach in order to mitigate local minima. The overall procedure for establishing the BO platform is summarized in Fig. 3a.

The established BO platform provides two major functions: (1) it can efficiently identify parameter combinations that consistently yield filaments with quality Q ranging from 3.1 to 3.3, indicating the formation of swelling, equivalent diameter, and stretched filaments for EIW of 3D structures (as shown in Fig. 3b); (2) it can rapidly screen and predict unknown parameters by plugging in the expected filament quality Q and the predefined parameters (as illustrated in Fig. 3c). As a result, the BO-enabled EIW requires substantially fewer experiments than traditional trial-and-error approaches, enabling efficient design of support bath materials and identification of optimal printing parameters.

2.3 Multi-objective BO and validation

To validate the functionality and predictive accuracy of the established BO platform, we conducted two series of optimizations under identical algorithmic settings but with different bound-expansion factors and random initializations. Specifically, the bound-expansion factors were varied between 1.0 and 1.5, allowing the optimizer to explore parameter values beyond the original ranges of X_i. In this way, we can achieve controlled extrapolation of the design space and improve robustness to potential bias in the initial dataset. The first series of optimizations aimed to predict suitable parameter combinations for printing well-defined filaments with Q values ranging from 3.1 to 3.3. The goal of the second optimization series was to explore the BO framework's ability to identify the formation of undesired filaments under the given conditions. The results of these tests are presented in Fig. 4a.

Each optimization began with broad exploration of the design space, producing a dense distribution of sampled points over a wide range of performance values. As the optimization progressed, sampling became increasingly concentrated in the high-performing regions identified by the Gaussian process surrogate and the EI acquisition function. The light green dots represent the evaluated candidate solutions sampled from one of four independent BO runs. The optimal solutions consistently lay near the upper envelope of the observed performance distribution, indicating that the optimization procedure can reliably guide the search toward high-quality parameter combinations in spite of the inherent stochasticity that arises from the random initialization and acquisition optimization. Meanwhile, the emergence of distinct clusters of optimal points suggests the presence of multiple high-performing local optima in the objective landscape, demonstrating robust identification of competitive solutions. In this work, we randomly selected 10 parameter combinations to form well-defined filaments and 5 parameter combinations to form defected filaments, which are marked by blue squares and red triangles, respectively. Then, to validate the predictive accuracy, three parameter combinations were chosen from these highlighted datasets in order to print filaments, as denoted in Fig. 4a.

Based on the target ink viscosities, we designed three ink materials composed of sodium alginate and poly(ethylene glycol) diacrylate (PEGDA) with different formulas. The viscosities of these ink materials were measured at different shear rates. The Carreau-Yasuda model [31] was applied to calculate the η_0 of each ink material as: $\eta(\dot{\gamma})=\eta_\infty+(\eta_0-\eta_\infty)(1+(\lambda\dot{\gamma})^a)^{(n-1)/a}$ (where η_∞ is the infinite viscosity, η_0 is the zero-shear-rate viscosity, λ is the relaxation time, $\dot{\gamma}$ is the shear rate, a is the transition parameter, and n is the flow behavior index), with results shown in Fig. 4b. After this,

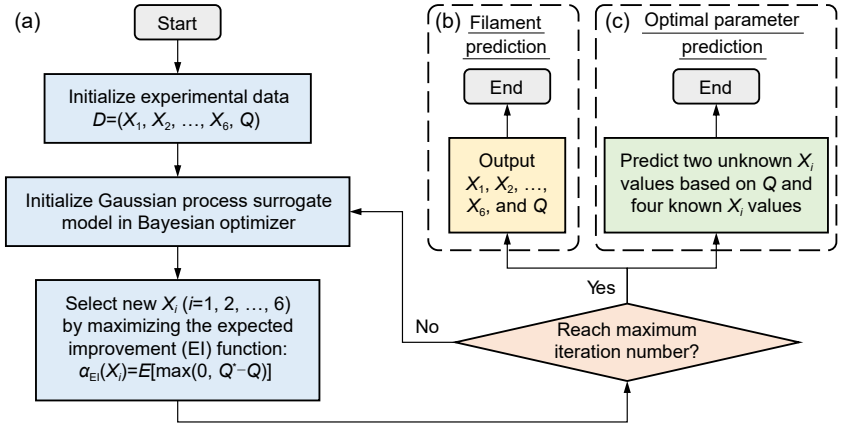

Fig. 3 Establishment of the Bayesian optimization (BO)-based filament prediction platform. (a) Flowchart to establish the BO platform for (b) filament prediction and (c) optimal parameter prediction

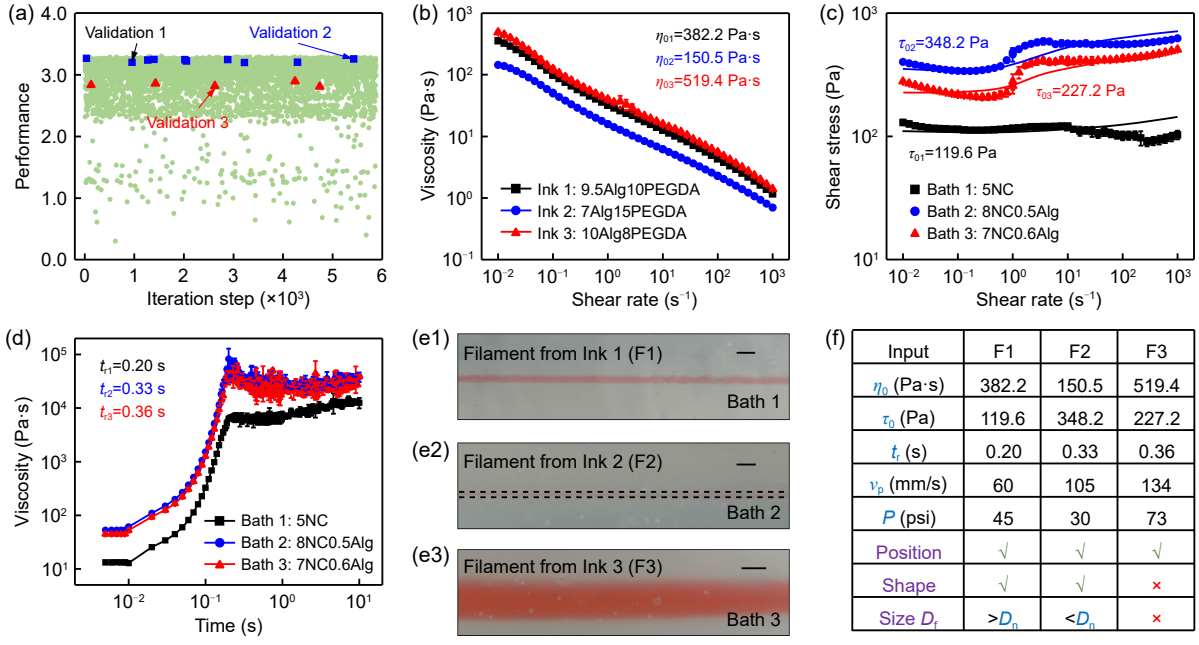

Input	F1	F2	F3
η_0 (Pa·s)	382.2	150.5	519.4
τ_0 (Pa)	119.6	348.2	227.2
t_r (s)	0.20	0.33	0.36
v_p (mm/s)	60	105	134
P (psi)	45	30	73
Position	√	√	√
Shape	√	√	×
Size D_f	>D_n	<D_n	×

Fig. 4 Multi-objective Bayesian optimization and validation through filament printing experiments. (a) Representative results from one of four independent Bayesian optimization runs with 10 randomly selected well-defined filaments denoted by blue squares, and five randomly selected defective filaments marked by red triangles. (b) Design of three inks with the η_0 values approximating the predictions, including Ink 1 (9.5% sodium alginate-10% poly(ethylene glycol) diacrylate (PEGDA), denoted as 9.5Alg10PEGDA), Ink 2 (7% sodium alginate-15% PEGDA, denoted as 7Alg15PEGDA), and Ink 3 (10% sodium alginate-8% PEGDA, denoted as 10Alg8PEGDA). Key rheological properties, τ_0 (c) and t_r (d), of three support bath materials to print filaments, including Bath 1 (5% nanoclay, denoted as 5NC), Bath 2 (8% nanoclay-0.5% sodium alginate, denoted as 8NC0.5Alg), and Bath 3 (7% nanoclay-0.6% sodium alginate, denoted as 7NC0.6Alg). (e) Filaments from three inks printed within corresponding support baths. Scale bars: 1.0 mm for (e1) and (e2), and 3.0 mm for (e3). (f) Summary of the experimental inputs and evaluation of the printed filaments via the position-shape-size (PSS) system. Data in (b–d) are expressed as mean±standard deviation (n=3)

three yield-stress fluids were selected as the support bath materials for filament printing, including 5% nanoclay, 8% nanoclay-0.5% sodium alginate, and 7% nanoclay-0.6% sodium alginate. In particular, the Herschel-Bulkley model [32] ($\tau = \tau_0 + k\dot{\gamma}^n$, where k is the consistency index) was utilized to calculate τ_0 for each support bath, as illustrated in Fig. 4c, while t_r was determined by monitoring the temporal viscosity variation at different shear rates (Fig. 4d). The key printing parameters (v_p, D_n, and P) were selected based on the optimization results.

Using these parameter combinations, three filaments were printed inside different support baths, with the processes recorded in Movie S1 (supplementary information). The results are also summarized in Fig. 4e. The filament made from Ink 1 exhibited a well-defined shape with a D_f value of 0.43 mm, as shown in Fig. 4e1, which was greater than the D_n value of 0.41 mm. Thus, it was determined to be a swelling filament, which was consistent with the theoretical prediction from the BO platform. The filament from Ink 2 also presented a good overall shape and circular cross-sectional shape, as illustrated in Fig. 4e2. No pronounced variations in position were observed after printing. We then measured the filament size and obtained a D_f value of 0.19 mm, being significantly lower than the D_n value of 0.33 mm. Therefore, this filament was categorized as a stretched filament, perfectly meeting the theoretical prediction (Q of 3.3).

The filament made from Ink 3 displayed an uncontrolled profile, with a measured diameter (D_f of 5.95 mm) that was substantially greater than the nozzle diameter D_n (1.20 mm), clearly demonstrating severe over-extrusion (Fig. 4e3). The BO platform, however, predicted a Q value of approximately 2.8, rather than the experimentally observed 2.2. This discrepancy likely arises from a nonlinear regime transition that was insufficiently sampled in the training dataset. Figure 4f summarizes the experimental inputs to print these three filaments as well as the evaluation results from the PSS system. Notably, the BO model correctly captured the overall statistical trends, that is, high viscosity, intermediate yield stress, and high path speed generally promote shape and diameter control. However, the simultaneous application of high P and long t_r in the case of Ink 3 likely triggered a pressure-dominated flow enhancement, resulting in an extrusion speed that significantly exceeded the path speed. Such threshold-like behavior represents a localized extrapolation beyond the densely sampled design space. Importantly, the predicted Q value of approximately 2.8 lay close to the boundary between the acceptable and over-extruded

regimes, suggesting that the BO platform can still provide physically reasonable predictions at the near-boundary area.

Overall, the platform proved itself reliable in screening for optimal parameter combinations for high-performance filament printing. In future work, additional experimental data may be incorporated to better sample the highly nonlinear failure regimes, thereby further improving the predictive accuracy for specific failure modes. For instance, in order to address the regime relevant to Ink 3, more experiments with high P and t_r values need to be performed to provide more data for enriching the BO platform.

2.4 Design of support bath using the BO platform

After validating the predictive accuracy of the platform, we used it to guide the design of support bath materials with desirable rheological properties. Herein, an alginate-based ink was developed, which was composed of sodium alginate and PEGDA. Sodium alginate is an ionically crosslinkable hydrogel. When divalent (e.g., calcium Ca^{2+} ions) or multivalent cations are applied, they bind to guluronic acid (G) blocks of alginate chains and form a classic "egg-box" microstructure among chains [33]. PEGDA is a photocurable hydrogel. Upon exposure to ultraviolet (UV) radiation in the presence of a photoinitiator, free radicals initiate chain growth at the acrylate double bonds, triggering free-radical polymerization and causing covalently crosslinked networks to form [1], as illustrated in Fig. 5a. When mixed, sodium alginate can effectively regulate the viscosity and biocompatibility of the ink, while PEGDA can precisely tune the mechanical properties of the ink following crosslinking [33, 34]. As a result, this alginate-based ink has been utilized for diverse biomedical applications, such as tissue reconstruction [35], in vitro disease modeling [36], and drug screening and toxicology testing [37].

Based on the preliminary tests, we used 9% and 10% as the sodium alginate and PEGDA concentrations, respectively. The viscosity of the alginate-based ink was measured in order to calculate its zero-shear-rate viscosity (η_{0alg}), as shown in Fig. 5b. Herein, we predefined the key printing parameters as follows: v_p=50 mm/s, D_n=0.41 mm, and P=60 psi. These parameters, along with η_{0alg}, served as the inputs to the BO platform to predict the optimal combinations of τ_0 and t_r, according to the procedure illustrated in Fig. 3c. After the optimization, we obtained 10 candidate combinations of these rheological properties that were used to design support baths. The combination highlighted in Fig. 5c was eventually chosen, which aimed to form stretched filaments in the target support bath.

Using these theoretical predictions, we designed a support bath with 4.5% Laponite RD nanoclay, which had a τ_{0RD} of 79.5 Pa (Fig. 5d) and t_{rRD} of 0.23 s (Fig. 5e); this was consistent with the predicted values and also provided

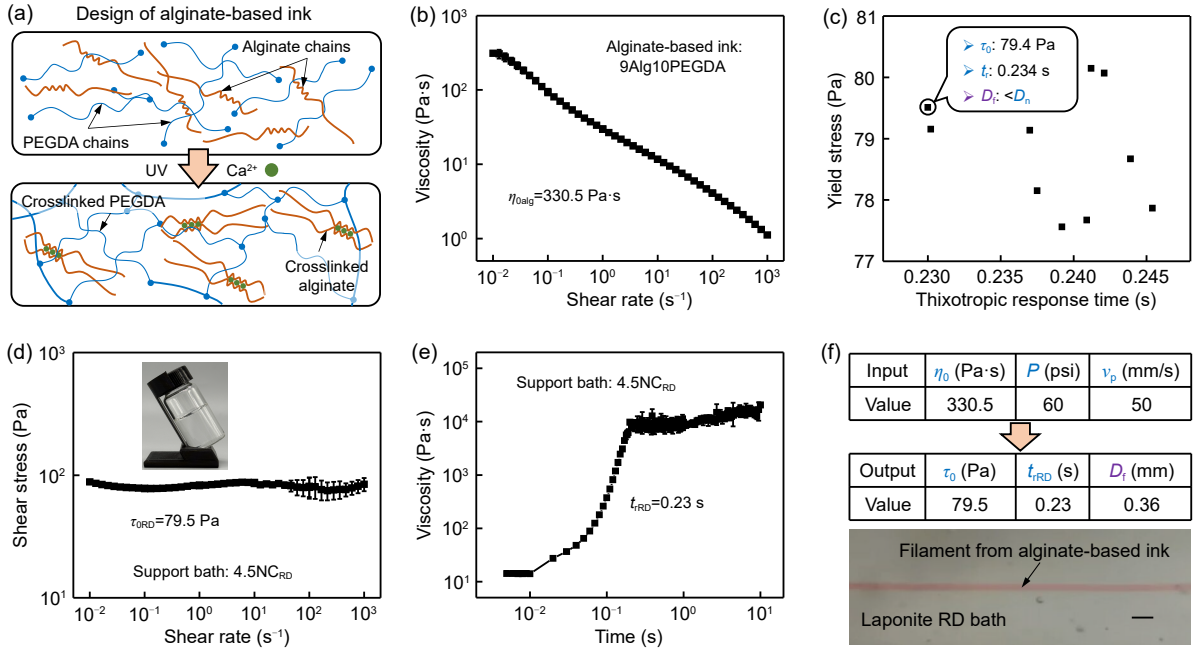

Fig. 5 Support bath design to print alginate-based ink. (a) Design of alginate-based ink composed of 9% sodium alginate and 10% poly(ethylene glycol) diacrylate (PEGDA) (9Alg10PEGDA), which can be crosslinked by both calcium ions (Ca^{2+}) and ultraviolet (UV) radiation. (b) Measurement of ink viscosity. (c) Prediction of the candidate combinations of support bath rheological properties. Rheological measurements, τ_0 (d) and t_r (e), of a designed support bath with 4.5% Laponite RD nanoclay ($4.5NC_{RD}$). Inset: the support bath with good transparency. (f) Key parameters and the stretched filament printed in the support bath. Scale bar: 1.0 mm. Data in (b, d, and e) are expressed as mean±standard deviation (n=3)

good transparency for the subsequent UV crosslinking (inset of Fig. 5d). Accordingly, a stretched filament was successfully printed in this support bath (Movie S2 in the supplementary information), which had a D_f of 0.36 mm, being lower than D_n (0.41 mm), as summarized in Fig. 5f. This result confirms that the established BO platform can effectively guide the design of support baths in order to achieve target rheological properties.

2.5 Identification of printing parameters using the BO platform

To identify optimal printing parameters using the BO platform, positively charged chitosan was used as the ink. Chitin/Chitosan is a naturally occurring copolymer of the β-(1-4)-linked co-polymers of *N*-acetyl-D-glucosamine and D-glucosamine [38]. Under acidic conditions, the amine groups ($–NH_2$) are protonated, converting neutral $–NH_2$ into positively charged $–NH_3^+$, which induces electrostatic repulsion between chitosan chains (as shown in Fig. 6a). Upon exposure to a specific salt solution (e.g., potassium carbonate (K_2CO_3) in this work), carbonate ions hydrolyze to generate hydroxide ions, thereby increasing the local pH above the acid dissociation constant of chitosan (pKa≈ 6.3 [39]), and inducing deprotonation of the protonated amine groups. This process eliminates the electrostatic repulsion between chitosan chains and promotes extensive inter- and intra-molecular hydrogen bonding and chain entanglement; these effects eventually result in the formation of a physically crosslinked chitosan network and make the chitosan states shift from liquid to solid, as presented in Fig. 6a. Due to their excellent biocompatibility and biodegradability, as well as tunable physicochemical properties, chitosan-based inks have been widely used for diverse applications such as drug delivery [39] and wound healing [40] in tissue engineering.

In this study, 3% chitosan ink was prepared and its viscosity was measured as shown in Fig. 6b. Accordingly, the zero-shear-rate viscosity (η_{0chi}) was computed as 5576.2 Pa·s. Laponite EP nanoclay was selected to formulate the support bath. Its organic modification reduces the pH sensitivity and enables stable miscibility with K_2CO_3. Thus, following deposition, chitosan filaments gradually underwent physical crosslinking in the support bath and eventually solidified. The τ_{0EP} and t_{rEP} of the support bath were measured as 7.9 Pa and 0.82 s, respectively, as illustrated in Figs. 6c and 6d, respectively. Specifically, organic modification of Laponite EP weakens electrostatic interactions between nanoclay platelets, resulting in a lower threshold stress for microstructural collapse, but an extended timescale for microstructural recovery compared with Laponite RD nanoclay at a similar concentration (e.g., $4.5NC_{RD}$ in Figs. 5d and 5e). Next, the ink viscosity and support bath rheological properties were input to the BO platform to predict the optimal combinations of v_p and P, using a dispensing nozzle with a D_n of 0.41 mm. After the optimization, we obtained 10 candidate

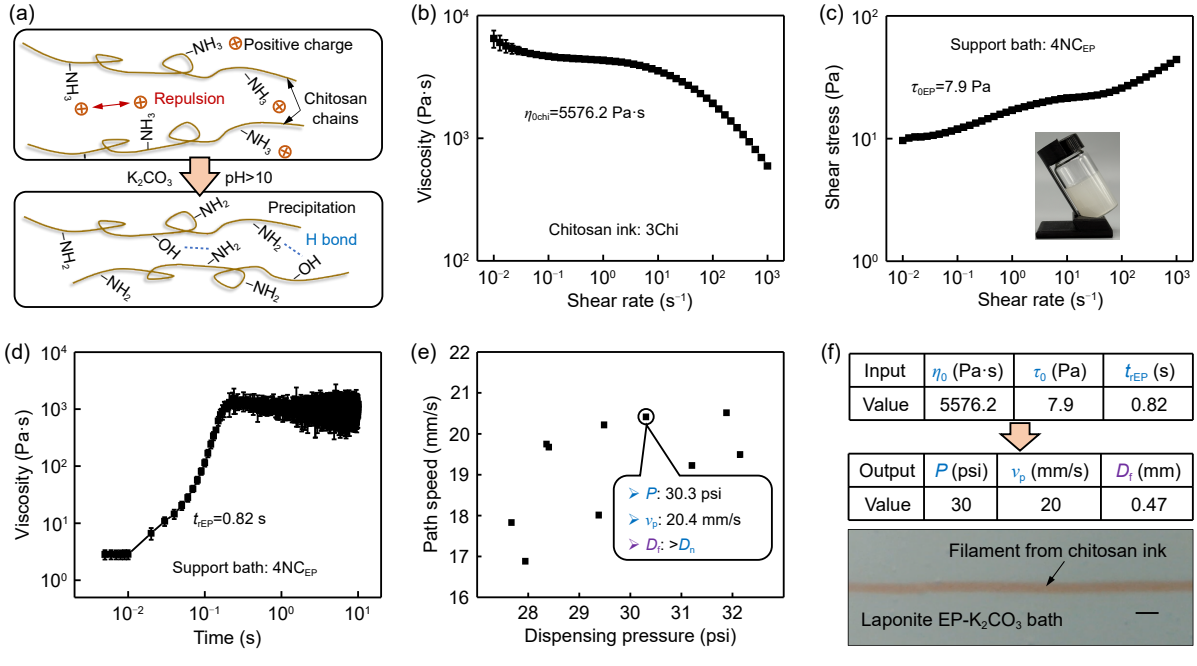

Fig. 6 Prediction of printing parameters for printing chitosan ink. (a) Design of chitosan ink which is crosslinkable via K_2CO_3. Rheological measurements of 3% chitosan ink (3Chi) viscosity (b), and τ_0 (c) and t_r (d) of the support bath with 4% Laponite EP nanoclay ($4NC_{EP}$, inset). (e) Prediction of the candidate combinations of the printing parameters P and v_p. (f) Key parameters and swelling filament printed in the support bath with 4% Laponite EP and 0.5% K_2CO_3. Scale bar: 1.0 mm. Data in (b–d) are expressed as mean±standard deviation (n=3)

parameter combinations, as illustrated in Fig. 6e. One of these sets (highlighted in Fig. 6e) was chosen to print swelling filaments from the chitosan ink in the support bath (recorded in Movie S3 in the supplementary information). The deposited filament is shown in Fig. 6f, which had a D_f of 0.47 mm (being greater than D_n), thus validating that the BO platform can accurately predict printing parameters that achieve well-defined filaments.

2.6 Efficient biofabrication of eye components using BO-enabled EIW

Using the designed support bath and the identified optimal printing parameters, two representative eye components—the tarsus and sclera—were biofabricated from the alginate-based ink and chitosan ink, respectively. We first created a tarsus model as shown in Fig. 7a1, which had overall dimensions of 27.68 mm×11.67 mm×1.02 mm. Based on the diameter of alginate filaments in Fig. 5f, the model was sliced into multiple layers in order to generate corresponding printing trajectories. Then, the printing was performed within the Laponite RD support bath, as illustrated in Fig. 7a2 and Movie S4 (supplementary information). Following printing, UV radiation was applied to chemically crosslink the printed tarsus, which was subsequently harvested from the support bath and submerged in a calcium chloride bath to promote ionic crosslinking with sodium alginate. The crosslinked tarsus (Fig. 7a3) had an overall size of 28.00 mm×13.55 mm×1.56 mm, which is close to the designed model. This engineered tarsus structure was then embedded within an eyelid (Fig. 7a4; Movie S5 in the supplementary information), which could be potentially used as a biomimetic scaffold to restore and support eyelid function, or as a patient-specific model for pre-surgical planning and training purposes [41–43].

Using a similar protocol, an engineered sclera structure was biofabricated via EIW. The digital model is presented in Fig. 7b1, which has a spherical shape with an outer diameter of around 18 mm, and a cornea diameter of about 9 mm. The model was printed from chitosan inside the Laponite EP support bath with 0.5% K_2CO_3, as shown in Fig. 7b2 and Movie S6 (supplementary information). Subsequent to printing, the structure was kept in the support bath for 5 h for initial crosslinking and then moved into a K_2CO_3 bath for full crosslinking, as depicted in Fig. 7b3. The crosslinked sclera had an outer diameter of around 19.1 mm, which was close to that of the digital model, validating its shape fidelity. Finally, this engineered sclera structure was integrated into a 3D-printed orbit model for demonstration, as illustrated in Fig. 7b4 and Movie S7 (supplementary information); it can potentially be used as a tissue-engineering scaffold for seeding scleral fibroblasts and/or stem cells in the study of scleral regeneration [40, 44, 45].

2.7 Discussion

The established BO platform exhibited relatively low predictive accuracy for defective filaments, which may be due to several factors. First, defective filaments originate from multiple competing failure mechanisms rather than a single stable formation mode. Although these outcomes are grouped under a common "defective" category, they remain mechanistically heterogeneous, making them inherently challenging for a single model to accurately learn and classify. Second, class imbalance within the dataset may bias the model toward the dominant category (i.e., the

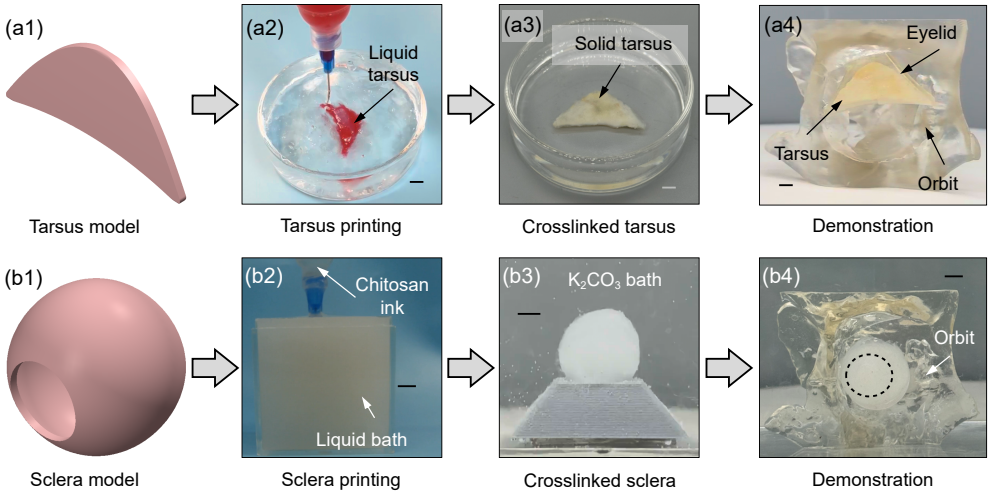

Fig. 7 Bayesian optimization-enabled embedded ink writing of eye components. (a1) Tarsus model, (a2) tarsus printing using the alginate-based ink, (a3) printed tarsus crosslinked via ultraviolet radiation and calcium chloride, and (a4) demonstration of the printed tarsus structure in an eyelid. (b1) Sclera model, (b2) sclera printing using the chitosan ink, (b3) printed chitosan crosslinked via K_2CO_3, and (b4) demonstration of the printed sclera structure in an orbit. Scale bars: 5.0 mm

well-defined filaments in this study), thereby reducing predictive performance for defective cases that are less represented in the data. Improvements could result from subdividing the defective category into mechanism-based classes, rather than treating all failure modes as a single label. This approach would also align better with the underlying physical interpretation established in this work. However, implementing such a strategy would require substantially larger experimental datasets that cover each defect-specific subgroup.

Nevertheless, the BO platform was demonstrated to effectively delineate a constrained region of rheological properties (Fig. 5c) and identify optimized combinations of printing parameters (Fig. 6e), thereby forming well-defined filaments in EIW. This capability reduces the need for time-consuming random experimentation. As a result, the development timeline for EIW of new inks can be shortened from several weeks or months to only a few days when employing the BO platform, thus enhancing design efficiency.

3 Conclusions

In this work, numerous filaments were printed via EIW and assessed through a PSS system. The obtained filament datasets, which encompassed six input variables (ink viscosity, support bath yield stress, thixotropic response time, path speed, nozzle diameter, and dispensing pressure), and one output variable (filament quality as evaluated by filament position, shape, and size), were utilized to establish the BO platform. The proposed platform could accurately predict the filament category when the input parameters were identified. Additionally, it promoted efficient design of the support bath and rapid selection of optimal printing parameters for new inks, which were validated by EIW tests with tarsus and sclera structures. This BO-enabled EIW offers a reliable, high-throughput method, paving the way for human tissue and organ reconstruction applications.

To simplify the BO platform, only the most important rheological properties were considered in this study. Other ink and support bath properties, such as the shear-thinning index, storage modulus, and relaxation time, will be incorporated into future BO platform iterations by training a new model using both the original descriptors and the added rheological features; this is a promising route for subsequent research since such features also play critical roles in governing filament morphology and geometry during EIW. In addition, the established BO platform is currently constrained to predicting hydrophilic ink printing within a hydrophilic support bath. For ink–support bath pairs with opposite affinities, interfacial behavior must be considered; future work on this topic would expand the applicative scope of the platform. Although the proposed BO platform was established with a necessary mechanistic basis to connect filament morphology and geometry to ink viscosity, bath rheological properties, and printing parameters, physics models were not integrated in the platform. In subsequent research, the platform can serve as a first step toward a framework that directly incorporates filament formation physics through physics-derived input descriptors, such as stress ratios, characteristic recovery times, and dimensionless ratios that compare nozzle transit time with support bath structural recovery time and other parameters. Such an approach will likely improve the predictive accuracy as well as advance our understanding of the underlying physics governing EIW. Another possible avenue is to modulate the current BO platform and use it to optimize printing paths; paths play a critical role in 3D bioprinting as they directly govern the mechanical properties of the printed constructs.

4 Materials and methods

4.1 Material preparation

The following support bath materials were used to print filaments. The nanoclay-Pluronic F127-PEGDA nanocomposite was prepared as per the protocol in Ref. [46], which was composed of nanoclay (Laponite RD, $Na_{0.7}Si_8Mg_{5.5}Li_{0.3}O_{20}(OH)_4$, BYK Additives Inc., Gonzales, TX, USA) at 3% (0.03 g/mL), Pluronic F127 (P2443, Sigma-Aldrich, Burlington, MA, USA) at 20% (0.2 g/mL), and PEGDA (Mn 700, Sigma-Aldrich, St. Louis, MO, USA) at 20% (volume fraction). The nanoclay-Pluronic F127 nanocomposites were prepared according to the protocol in Ref. [34], with nanoclay concentrations of 2%, 3%, and 4% (0.02, 0.03, and 0.04 g/mL) and Pluronic F127 concentrations of 10%, 20%, 30%, and 35% (0.10, 0.20, 0.30, and 0.35 g/mL). The nanoclay-NaAlg nanocomposites were prepared as per the protocol in Ref. [1], with nanoclay concentrations of 4% and 6% (0.04 and 0.06 g/mL) and NaAlg ($NaC_6H_7O_6$, Sigma-Aldrich, Burlington, MA) concentrations of 0.25%, 0.5%, 1%, 1.5%, and 4% (0.0025, 0.005, 0.01, 0.015, and 0.04 g/mL). The nanoclay-PEGDA nanocomposites were prepared by following the procedure in Ref. [1], using nanoclay concentrations of 2%, 6%, and 8% (0.02, 0.06, and 0.08 g/mL) and PEGDA concentrations of 10% and 20% (volume fraction). The nanoclay suspensions were prepared according to the protocol in Ref. [33], with nanoclay concentrations of 2%, 3%, 4%, and 6% (0.02, 0.03, 0.04, and 0.06 g/mL). All preparations were performed at room temperature. Moreover, all support baths were degassed using a centrifuge (Cole-Parmer VS3400, Cole-Parmer Instrument Company, Vernon Hills, IL, USA) at 3000 r/min for 5 min. After removing entrapped air bubbles, the support baths were stored in sealed containers at room temperature for one day of aging prior to use.

The ink materials for filament printing included NaAlg-PEGDA solutions with NaAlg concentrations of 5% and 10% (0.05 and 0.10 g/mL) and PEGDA concentrations of 10% and 15% (volume fraction) as per the protocol in Ref. [1], gelatin (Emprove Essential, Sigma-Aldrich, St. Louis, MO, USA) solutions with concentrations of 1%, 2.5%, and 5% (0.01, 0.025, and 0.05 g/mL) following the protocol in Ref. [47], Pluronic F127 solutions with concentrations of 30% and 40% (0.3 and 0.4 g/mL) according to the protocol in Ref. [48], nanoclay-NaAlg nanocomposites with nanoclay concentrations of 6% and 8% (0.06 and 0.08 g/mL) and NaAlg concentrations of 1% and 4% (0.01 and 0.04 g/mL) as per the procedure in Ref. [1], and nanoclay-Pluronic F127 nanocomposite with a nanoclay concentration of 2% (0.02 g/mL) and Pluronic F127 concentration of 0.25% (0.0025 g/mL), again following the protocol in Ref. [1]. After preparation, the ink materials were degassed using the centrifuge at 3000 r/min for 2 min, thus removing air bubbles. For the ink materials containing nanoclay, one-day aging at room temperature was necessary before use.

The alginate-based ink for printing tarsus structures was prepared by dispersing 9% (0.09 g/mL) NaAlg powders into 10% (volume fraction) PEGDA solution, and then mixing using an overhead stirrer (50006-03, Cole-Parmer Instrument Company, Vernon Hills, IL) at 800 r/min for 1 h. Before adding NaAlg, 0.1% (0.001 g/mL) photoinitiator I2959 (2-hydroxy-4'-(2-hydroxyethoxy)-2-methylpropiophenone, Sigma-Aldrich, Burlington, MA) was dispersed into the PEGDA solution and mixed for 5 min using the overhead stirrer. A red colored dye (McCormick & Co., Inc., Hunt Valley, MD, USA) was added at 0.01% (volume fraction) to enhance visibility. The support bath for printing this ink was prepared by dissolving Laponite RD nanoclay in deionized (DI) water at 4.5% (0.045 g/mL). The suspension was then aged for one day before use. To prepare the chitosan ink, crustacean shell chitosan powder was obtained from Tokyo Chemical Industry Co. Ltd. (Japan) and further deacetylated using hot sodium hydroxide under 120 °C for 3 h under nitrogen reflux, to a degree of deacetylation above 90% as measured by titration. Deacetylated chitosan powder was washed with DI water 3–4 times and air-dried prior to the ink formulation. Then, the chitosan powder was added to 2% (volume fraction) acetic acid solution (CH_3CO_2H, ≥99%, Sigma-Aldrich, St. Louis, MO) at a concentration of 3% (0.03 g/mL), and dissolved by manually mixing the solution with a stirring rod for 10 min. The support bath for printing this chitosan ink was prepared by dissolving Laponite EP nanoclay in DI water at 4% (0.04 g/mL). Furthermore, potassium carbonate (K_2CO_3, Sigma-Aldrich, St. Louis, MO) was added to the suspension at 0.5% (0.005 g/mL). The mixing process was performed using the overhead stirrer at 800 r/min for 90 min. All operations were conducted at room temperature.

4.2 Characterization of rheological properties

A rheometer (MCR 92, Anton Paar, Ashland, VA, USA) with a cone-plate measuring system (cone angle of 1°, cone diameter of 50 mm, and cone-to-plate gap of 0.102 mm) was used to characterize the yield stress and thixotropic response time of the support baths as well as the viscosity of the ink materials. In particular, steady shear rate sweeps were conducted to measure the yield stress values of support baths, wherein the shear rate was increased from 0.01 to 1000 s^{-1} and the shear stress was recorded. Transient step shear rate sweeps were performed to quantify the thixotropic response time. In these measurements, the support baths were pre-sheared at a relatively high shear rate of 10 s^{-1} for 200 s and then sheared at a low shear rate of 0.01 s^{-1}. The variation of viscosity was recorded for 1000 s. All measurements were performed at room temperature. For the ink materials, steady shear rate sweeps were conducted in order to measure the viscosities by increasing the shear rate from 0.01 to 1000 s^{-1}. For the gelatin solutions, the steady shear rate sweeps were performed at both room temperature and 37 °C. For all other inks, the viscosity was measured at room temperature.

4.3 Filament printing and data collection

To collect sufficient filaments for establishing the BO platform, the inks were printed in diverse support baths at different pressures (ranging from 5 to 60 psi), path speeds (ranging from 1 to 100 mm/s), and nozzle diameters (0.20, 0.25, 0.35, 0.43, 0.63, and 0.86 mm). To improve visibility, a red colored dye (McCormick & Co., Inc., Hunt Valley, MD) was added to the inks at 0.01% (0.0001 g/mL). A camera (120 frames/s USB camera, ELP, Shenzhen, China) was placed in front of the support baths to record the filament formation. Following printing, the filament position, shape, and size were evaluated to determine the filament type. In particular, the filament size was measured using ImageJ software (National Institutes of Health, Bethesda, MD, USA) based on the videos recorded by the camera. By varying the combination of support baths, ink materials, and printing parameters, a total of 1018 filaments were printed and assessed. To validate the theoretical predictions, the alginate-based ink was printed in the Laponite RD nanoclay bath at a path speed of 50 mm/s, nozzle diameter of 0.41 mm, and dispensing pressure of 60 psi. The chitosan ink was printed in the Laponite EP-K_2CO_3 bath at a path speed of 20 mm/s, nozzle diameter of 0.41 mm, and dispensing pressure of 30 psi.

4.4 Establishing the BO platform

To establish the BO platform, an initial training dataset was generated using Latin hypercube sampling so as to ensure

good space-filling coverage. After each iteration of the optimization, the surrogate model was retrained with the expanded dataset to improve its predictive accuracy. Each iteration of the Bayesian optimization loop included: (1) identifying a candidate parameter set using the expected improvement acquisition function, (2) conducting a filament embedded printing experiment under the proposed conditions, (3) evaluating the resulting filament based on the PSS system in order to assign a Q value, and (4) updating the surrogate model. The optimization proceeded until the improvements in Q^* became negligible. Based on the predictions from the platform, filaments were printed from diverse inks in the support baths with the desired rheological properties. The filament Q values were assessed using the PSS system and compared to the theoretical predictions to validate the platform's effectiveness.

4.5 Printing of complex 3D structures

The same alginate-based ink and chitosan ink were utilized to print the tarsus and sclera structures, respectively, within the corresponding support baths. The printing parameters for both inks were consistent with those used for filament printing. A homemade extrusion 3D printing system modified based on a fused deposition modeling 3D printer (SOVOL 3D, Shenzhen Liandian Technology Co., Ltd., Shenzhen, China) was applied to print the structures at room temperature. The models were created using SolidWorks software (Dassault Systèmes SolidWorks Corp., Waltham, MA, USA) and then converted into .STL files. After printing, the tarsus structure inside the support bath was exposed to UV radiation from a UV curing system (OmniCure Series 2000, wavelength: 320–500 nm, Lumen Dynamics, Mississauga, ON, Canada) for 15 min and then harvested from the support bath, which was subsequently submerged in a 2.0% (0.02 g/mL) calcium chloride (C8106, Sigma-Aldrich, Burlington, MA) solution for 1 h to cause ionic crosslinking. The sclera structure was kept inside the support bath for 5 h for crosslinking and then moved into a 0.5% (0.005 g/mL) K_2CO_3 bath for 2 h for complete crosslinking. The camera was used to record both the printing process and structure demonstration.

4.6 Statistical analysis

All quantitative values of measurement in the figures were reported as mean±standard deviation with n=3 samples per group.

Supplementary Information The online version contains supplementary material available at https://doi.org/10.1631/bdm.2600114.

Acknowledgements Biopolymer preparation and coagulation research were conducted as part of a user project at the Center for Nanophase Materials Sciences (CNMS), which is a US Department of Energy, Office of Science User Facility at Oak Ridge National Laboratory. Special acknowledgment was given to Dr. Weijian Hua at Texas A&M University for his assistance in collecting filament data. LR would like to acknowledge the support of the National Science Foundation Graduate Research Fellowship Program through Nevada System of Higher Education (NSHE) sub-award number: AWD0002282-1937966. YW acknowledges the support of the National Science Foundation (No. OIA 2033424). BD and YFJ acknowledge the support of the National Science Foundation (Nos. 2515837 and 2515838).

Author contributions SQ: methodology, formal analysis, investigation, data curation, visualization, writing—original draft preparation, and writing—review & editing. HRC: methodology, formal analysis, investigation, data curation, visualization, writing—original draft preparation, and writing—review & editing. LR: methodology, formal analysis, investigation, and writing—review & editing. ES: methodology, formal analysis, and investigation. HT: methodology. LB: methodology. YY: methodology, formal analysis, investigation, conceptualization, and writing—review & editing. BD: conceptualization, writing—review & editing, supervision, and project administration. YW: conceptualization, writing—review & editing, supervision, and project administration. GRC: conceptualization, writing—review & editing, supervision, and project administration. YFJ: conceptualization, writing—original draft preparation, writing—review & editing, supervision, and project administration.

Declarations

Conflict of interest YFJ is an associate editor of *Bio-Design and Manufacturing* and was not involved in the editorial review or the decision to publish this article. The authors declare that they have no known competing financial interests or personal relationships that could have appeared to influence the work reported in this paper.

Ethical approval This article does not contain any studies with human participants or animals performed by any of the authors. Therefore, ethical approval was not required.

Data availability All data that support the findings of this study are included within the article. Additional data are available from the corresponding author (yifeij@unr.edu) upon reasonable request.

Use of generative AI tools During the preparation of this work, the authors did not use any generative AI tools or services in the writing or editing process.

References

1. Hua WJ, Zhang C, Cui HR et al (2025) High-speed embedded ink writing of anatomic-size organ constructs. *Adv Sci* 12(13): 2405980. https://doi.org/10.1002/advs.202405980
2. Karyappa R, Ching T, Hashimoto M (2020) Embedded ink writing (EIW) of polysiloxane inks. *ACS Appl Mater Interfaces* 12(20): 23565–23575. https://doi.org/10.1021/acsami.0c03011
3. Zhang YX, Pang TQ, Sun ZX et al (2025) Up-and-down transformable embedded ink writing strategy for soft 3D architectures. *Nat Commun* 16:11348. https://doi.org/10.1038/s41467-025-66418-z
4. Hua WJ, Zhang C, Mitchell K et al (2024) Filament formation mechanisms in yield-stress fluid-enabled embedded ink writing.

Addit Manuf 91:104353.
https://doi.org/10.1016/j.addma.2024.104353
5. Colanges S, Tourvieille JN, Lidon P et al (2023) 2.5D printing of a yield-stress fluid. *Sci Rep* 13:5155.
https://doi.org/10.1038/s41598-023-32007-7
6. Friedrich LM, Gunther RT, Seppala JE (2022) Suppression of filament defects in embedded 3D printing. *ACS Appl Mater Interfaces* 14(28):32561–32578.
https://doi.org/10.1021/acsami.2c08047
7. Friedrich LM, Seppala JE (2021) Simulated filament shapes in embedded 3D printing. *Soft Matter* 17(35):8027–8046.
https://doi.org/10.1039/d1sm00731a
8. Karyappa R, Liu HF, Zhu Q et al (2023) Printability of poly(lactic acid) ink by embedded 3D printing via immersion precipitation. *ACS Appl Mater Interfaces* 15(17):21575–21584.
https://doi.org/10.1021/acsami.3c00149
9. Cho JH, Dressaire E (2024) Spreading of low-viscosity ink filaments driven by bath viscoelasticity in embedded printing. *Phys Rev Appl* 22(3):034050.
https://doi.org/10.1103/physrevapplied.22.034050
10. Friedrich LM, Woodcock JW (2024) Filament disturbance and fusion during embedded 3D printing of silicones. *ACS Biomater Sci Eng* 10(10):6690–6710.
https://doi.org/10.1021/acsbiomaterials.4c01014
11. Zhang C, Hua WJ, Juarez K et al (2025) Ink-bath interactions in embedded ink writing for producing functional parts. *Adv Mater Technol* 10(6):2401693.
https://doi.org/10.1002/admt.202401693
12. Sauret A, Ray TR, Compton BG (2026) Fluid mechanics challenges in direct-ink-writing additive manufacturing. *Annu Rev Fluid Mech* 58:413–442.
https://doi.org/10.1146/annurev-fluid-100224-111013
13. Guan JA, Sun YZ, Yao EJ et al (2025) Machine learning-assisted stiffness prediction in high-cell-density bioprinting. *Bio-Des Manuf* 8(4):543–557.
https://doi.org/10.1631/bdm.2400454
14. Shin J, Lee Y, Li ZK et al (2022) Optimized 3D bioprinting technology based on machine learning: a review of recent trends and advances. *Micromachines* 13(3):363.
https://doi.org/10.3390/mi13030363
15. Bai L, Zhang Y, Wang SC et al (2026) Artificial intelligence-enabled bioprinting 5.0. *Bio-Des Manuf* 9(1):32–62.
https://doi.org/10.1631/bdm.2400354
16. Zhao WX, Hu CX, Wang YN et al (2025) Optimization-based conformal path planning for in situ bioprinting during complex skin defect repair. *Bio-Des Manuf* 8(1):1–19.
https://doi.org/10.1631/bdm.2300365
17. Brunel LG, Hull SM, Heilshorn SC (2022) Engineered assistive materials for 3D bioprinting: support baths and sacrificial inks. *Biofabrication* 14(3):032001.
https://doi.org/10.1088/1758-5090/ac6bbe
18. Zhou K, Sun YD, Yang JQ et al (2022) Hydrogels for 3D embedded bioprinting: a focused review on bioinks and support baths. *J Mater Chem B* 10(12):1897–1907.
https://doi.org/10.1039/d1tb02554f
19. Jiang JH, Yuan CH, Zhang XY et al (2024) 3D bioprinting of liquid high-cell-proportion bioinks in liquid granular bath. *Adv Mater* 36(49):2412127.
https://doi.org/10.1002/adma.202412127
20. Navara AM, Xu YL, Perez MR et al (2024) Aspects of a suspended bioprinting system affect cell viability and support bath properties. *Tissue Eng Part A* 30(11–12):256–269.
https://doi.org/10.1089/ten.TEA.2023.0097
21. Lee JM, Yeong WY (2016) Design and printing strategies in 3D bioprinting of cell-hydrogels: a review. *Adv Healthc Mater* 5(22):2856–2865.
https://doi.org/10.1002/adhm.201600435
22. Schwab A, Levato R, D'Este M et al (2020) Printability and shape fidelity of bioinks in 3D bioprinting. *Chem Rev* 120(19):11028–11055.
https://doi.org/10.1021/acs.chemrev.0c00084
23. Adhikari J, Roy A, Das A et al (2021) Effects of processing parameters of 3D bioprinting on the cellular activity of bioinks. *Macromol Biosci* 21(1):2000179.
https://doi.org/10.1002/mabi.202000179
24. Hua WJ, Mitchell K, Raymond L et al (2021) Fluid bath-assisted 3D printing for biomedical applications: from pre- to postprinting stages. *ACS Biomater Sci Eng* 7(10):4736–4756.
https://doi.org/10.1021/acsbiomaterials.1c00910
25. He Y, Yang FF, Zhao HM et al (2016) Research on the printability of hydrogels in 3D bioprinting. *Sci Rep* 6:29977.
https://doi.org/10.1038/srep29977
26. Lamberger Z, Schubert DW, Buechner M et al (2024) Advanced optical assessment and modeling of extrusion bioprinting. *Sci Rep* 14:13972.
https://doi.org/10.1038/s41598-024-64039-y
27. Fu ZQ, Naghieh S, Xu CC et al (2021) Printability in extrusion bioprinting. *Biofabrication* 13(3):033001.
https://doi.org/10.1088/1758-5090/abe7ab
28. Wu J, Chen XY, Zhang H et al (2019) Hyperparameter optimization for machine learning models based on Bayesian optimization. *J Electron Sci Technol* 17:26–40.
https://doi.org/10.11989/JEST.1674-862X.80904120
29. Wang TT, Wang XP, Ma RZ et al (2020) Random forest-Bayesian optimization for product quality prediction with large-scale dimensions in process industrial cyber–physical systems. *IEEE Internet Things J* 7(9):8641–8653.
https://doi.org/10.1109/JIOT.2020.2992811
30. Cho HU, Nam Y, Choi EJ et al (2021) Comparative analysis of the optimized ANN, SVM, and tree ensemble models using Bayesian optimization for predicting GSHP COP. *J Build Eng* 44:103411.
https://doi.org/10.1016/j.jobe.2021.103411
31. Calafel MI, Criado-Gonzalez M, Aguirresarobe R et al (2025) From rheological concepts to additive manufacturing assessment of hydrogel-based materials for advanced bioprinting applications. *Mater Adv* 6(14):4566–4597.
https://doi.org/10.1039/D5MA00019J
32. Tumbic J, Ferrarese E, Martinez R et al (2025) Particle-based hydrogel inks and support matrices for biofabricating structural complexity, soluble gradients, and cell-lined channels in fully granular bioprinted systems. *Biofabrication* 17(4):045015.
https://doi.org/10.1088/1758-5090/adfe97
33. Hua WJ, Zhang C, Mitchell K et al (2025) Advanced design and 3D printing strategies with alginate-nanoclay nanocomposites: from microstructure to bioprinting. *Adv Mater Technol* 10(5):2401167.
https://doi.org/10.1002/admt.202401167
34. Zhang C, Hua WJ, Mitchell K et al (2024) Multiscale embedded printing of engineered human tissue and organ equivalents. *Proc Natl Acad Sci USA* 121(9):e2313464121.
https://doi.org/10.1073/pnas.2313464121
35. Liu YH, Ding AX (2025) An overview of recent advancements in 4D printing of alginate hydrogels for tissue regeneration. *J Biomater Sci Polym Ed* 36(18):2786–2819.
https://doi.org/10.1080/09205063.2025.2509031
36. Li JF, Hietel B, Brunk MGK et al (2025) 3D-printed microstructured alginate scaffolds for neural tissue engineering. *Trends Biotechnol* 43(2):447–461.
https://doi.org/10.1016/j.tibtech.2024.10.013

37. Geevarghese R, Somasekharan LT, Bhatt A et al (2022) Development and evaluation of a multicomponent bioink consisting of alginate, gelatin, diethylaminoethyl cellulose and collagen peptide for 3D bioprinting of tissue construct for drug screening application. *Int J Biol Macromol* 207:278–288. https://doi.org/10.1016/j.ijbiomac.2022.02.191
38. Taghizadeh M, Taghizadeh A, Yazdi MK et al (2022) Chitosan-based inks for 3D printing and bioprinting. *Green Chem* 24(1): 62–101. https://doi.org/10.1039/D1GC01799C
39. Rostami E (2022) Chitosan-based nanoparticles for drug delivery. In: Jana S, Jana S (Eds.), Nanoengineering of Biomaterials (1st Ed.). Wiley, Hoboken, p.1–32. https://doi.org/10.1002/9783527832095.ch1
40. Han L, Liu ZX, Li M et al (2025) 3D bioprinting of a dermal scaffold for full-thickness skin tissue regeneration. *Bio-Des Manuf* 8(1):68–84. https://doi.org/10.1631/bdm.2400058
41. Liu JC, Zhang MG, Zhou ML et al (2026) Exploring biomaterial scaffolds for eyelid reconstruction: a synthesis of experimental findings. *Tissue Eng Part B Rev* 32(2):143–156. https://doi.org/10.1089/ten.teb.2024.0364
42. Mahmoudsalehi AO, Soleimani M, Rios KSC et al (2025) Advanced 3D scaffolds for corneal stroma regeneration: a preclinical progress. *J Mater Chem B* 13(21):5980–6020. https://doi.org/10.1039/D5TB00090D
43. Sokmen S, Cakmak S, Oksuz I (2024) 3D printing of an artificial intelligence-generated patient-specific coronary artery segmentation in a support bath. *Biomed Mater* 19(3):035038. https://doi.org/10.1088/1748-605X/ad3f60
44. Mousavi Z, Bagheri M, Rostaminasab G et al (2024) Tissue engineering strategies for ocular regeneration; from bench to the bedside. *Heliyon* 10(20):e39398. https://doi.org/10.1016/j.heliyon.2024.e39398
45. Xue Q, Ma L, Hu HY et al (2023) 3D bioprinting as a prospective therapeutic strategy for corneal limbal epithelial stem cell deficiency. *Int J Bioprinting* 9(3):710. https://doi.org/10.18063/ijb.710
46. Hua WJ, Zhang C, Raymond L et al (2025) Embedded 3D printing of engineered lung cancer model for assisting fine-needle aspiration biopsy. *Biofabrication* 17(1):015042. https://doi.org/10.1088/1758-5090/ad9fe0
47. Hua WJ, Zhang C, Raymond L et al (2023) 3D printing-based full-scale human brain for diverse applications. *Brain X* 1(1):e5. https://doi.org/10.1002/brx2.5
48. Hua WJ, Mitchell K, Raymond L et al (2023) Embedded 3D printing of PDMS-based microfluidic chips for biomedical applications. *J Manuf Sci Eng* 145:011002. https://doi.org/10.1115/1.4055323